Ion-loss events in a hybrid trap of cold Rb-Ca+: Photodissociation, blackbody radiation, and nonradiative charge exchange

Xiaodong Xing [1], Humberto da Silva, Jr. [1,2], Romain Vexiau [1], Nadia Bouloufa-Maafa [1],
Stefan Willitsch [3], and Olivier Dulieu [1,*]

[1] *Université Paris-Saclay, CNRS, Laboratoire Aimé Cotton, 91405 Orsay, France*
[2] *Department of Chemistry and Biochemistry, University of Nevada, Las Vegas, 89154 Nevada, USA*
[3] *Department of Chemistry, University of Basel, Klingelbergstrasse 80, 4056 Basel, Switzerland*

We theoretically investigate the collisional dynamics of laser-cooled ^{87}Rb ground-state atoms and ^{40}Ca$^+$ ground-state ions in the context of the hybrid trap experiment of Hall *et al.* [Phys. Rev. Lett. **107**, 243202 (2011)], leading to ion losses. Cold ^{87}Rb^{40}Ca$^+$ ground-state molecular ions are created by radiative association, and we demonstrate that they are protected against photodissociation by blackbody radiation and by the ^{40}Ca$^+$ cooling laser at 397 nm. This paper yields an interpretation of the direct observation of ^{87}Rb^{40}Ca$^+$ ions in the experiment, in contrast to other hybrid trap experiments using other species. Based on an updated model for molecular spin-orbit interaction, we also confirm that the nonradiative charge-exchange is the dominant loss process for Ca$^+$ and obtain rates in agreement with experimental observations and a previous calculation.

I. INTRODUCTION

In the research field of ultracold dilute matter (namely, when the kinetic energy of the particles is well below $k_B \times$ 1 mK and the density does not exceed 10^{15} cm^{-3}, k_B being the Boltzmann constant), the development of so-called hybrid traps, which merge ultracold atoms and atomic ions opened fascinating topics [1]: the premises of cold chemistry with the formation of cold molecular ions [2–7], the dynamics of ultracold inelastic collisions and charge exchange between ground-state atoms and excited-state ions involving large internal energy [8–14], the dominant character of ultracold three-body collisions between an ion and two atoms [15,16] due to the long-range ion-atom interaction, the enhancement of ion cooling induced by resonant charge exchange [17,18], the emergence of ultracold ion-atom collisions in the quantum regime [19] with the observation of spin-exchange [20] and Feshbach resonances [21]. The advantage of such atom-ion experiments is that the detection of charged particles yields reliable fingerprints to distinguish among various possible reaction channels. In all the corresponding experimental situations, the unavoidable presence of lasers to cool and trap the species has been probed to have large consequences on the hybrid trap dynamics. For instance, the detection of the above-mentioned inelastic collisions originates from the creation of excited ions during the laser-cooling process [2,22]. Cold molecular ions are also expected to be mostly destroyed by these lasers [23].

The direct observation of cold molecular ions has been reported in experiments involving a magneto-optical trap (MOT) of ^{87}Rb atoms and a Paul trap of ^{40}Ca$^+$ [2,4] or ^{138}Ba$^+$ ions [5]. In these experiments, molecular ions were detected via mass spectrometry performed in the Paul trap, including RbCa$^+$, RbBa$^+$, and also Rb$_2^+$. In Ref. [7], the life and death of weakly bound RbBa$^+$ ions produced by three-body collisions is inferred from the observation of the survival of a single Ba$^+$ ion embedded in an ultracold Rb quantum gas. Finally, while not directly observed, the formation of YbCa$^+$ [24] and BaCa$^+$ [22] ions is invoked to interpret the corresponding experimental results.

To further clarify the direct observation of ^{87}Rb^{40}Ca$^+$ species in Refs. [2,4], we present in this paper an extension of our previous theoretical study devoted to radiative association (RA) of laser-cooled ^{87}Rb atoms and alkaline-earth ions [25] (hereafter referred to as paper I), invoking the processes schematized in Fig. 1. We model the photodissociation (PD) of the presumably formed ground-state ^{87}Rb^{40}Ca$^+$ ions by the lasers present in the experiment of Refs. [2,4]. We also evaluate the role of blackbody radiation (BBR) in the evolution of the vibrational distribution of the ^{87}Rb^{40}Ca$^+$ ions. As our study relies on updated molecular data compared to paper I, namely, the calculation of the molecular spin-orbit couplings (SOCs) using a quasidiabatic approach [26], we assess their validity by computing the rate for SOC-induced nonradiative charge exchange (NRCE), which has been found to be the dominant process (in particular, over RA) [27,28] in the experiment of Ref. [2], by comparison with radiative charge exchange (RCE) and RA. Our paper complements the recent theoretical investigation of Ref. [29].

The paper is organized as follows. We first present the molecular data in Sec. II, including the main features of the quasidiabatic approach for SOC. Then, in Sec. III, we recall the expected vibrational population of the RbCa$^+$ molecular ions created by RA and investigate its possible redistribution induced by BBR. Then the main result of this paper is reported in Sec. IV, where we show that the created molecular ions are protected against photodissociation in the experiment. Finally, Sec. V revis-

---

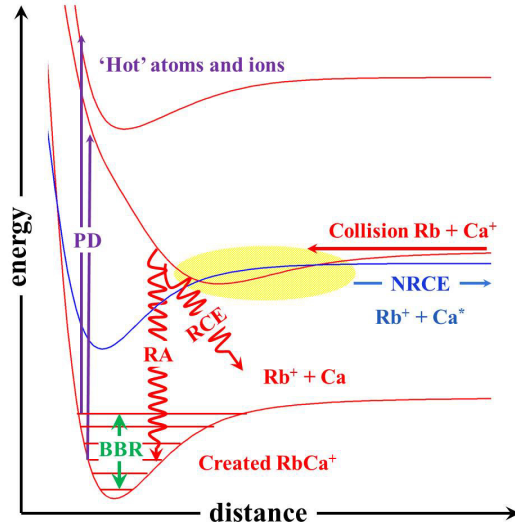*olivier.dulieu@universite-paris-saclay.fr

FIG. 1. The expected dynamical processes when a Rb atom and a Ca^+ ion, both in their ground state, collide at low energies (horizontal red arrow): NRCE (nonradiative charge exchange) yielding a Rb^+ ion and an excited-state Ca^* atom; RCE (radiative charge exchange) yielding a Rb^+ ion and a ground-state Ca atom; RA (radiative association) creating a cold ground-state molecular ion; BBR (blackbody radiation) redistributing the population of the rovibrational levels of $RbCa^+$; PD (photodissociation) induced by the cooling lasers, producing excited-state Rb^*/Ca^* atoms and Rb^+/Ca^+ ions with outgoing energies depending on the reached dissociation threshold.

its the NRCE, with the occurrence of a phase-matching condition which significantly influences the description of the process.

II. POTENTIAL ENERGY CURVES, ELECTRIC DIPOLE MOMENTS, AND SPIN-ORBIT COUPLINGS

The potential energy curves (PECs), transition electric dipole moments (TEDMs), and permanent electric dipole moments (PEDMs) for numerous electronic states are calculated following the methodology and parameters described in Refs. [30,31] and already used in paper I. In a few words, it consists of using the CIPSI (CONFIGURATION INTERACTION BY PERTURBATION OF A MULTICONFIGURATION WAVE FUNCTION SELECTED ITERATIVELY) program [32]. The diatomic molecular ion is modeled as an effective two-valence-electron system with effective core potentials (ECP) from Ref. [33], complemented with core-polarization potentials (CPP) [34] parametrized according to the angular momentum of the valence electron as in Ref. [35]. Two large Gaussian basis sets are employed, centered on each ionic core (namely, Rb^+ and Ca^{2+} here). A full configuration interaction (FCI) is then achieved to obtain from the same calculation the properties of the electronic ground state and of many excited electronic states of various symmetries with the same numerical accuracy. More details are provided in the Appendix.

The energies of the eight lowest dissociation limits of $RbCa^+$ are listed in the Appendix for the sake of clarity. By construction, our values are found to be very close to the experimental values for the $Rb(5s\,^2S)+Ca^+(nl\,^2L)$ limits, as
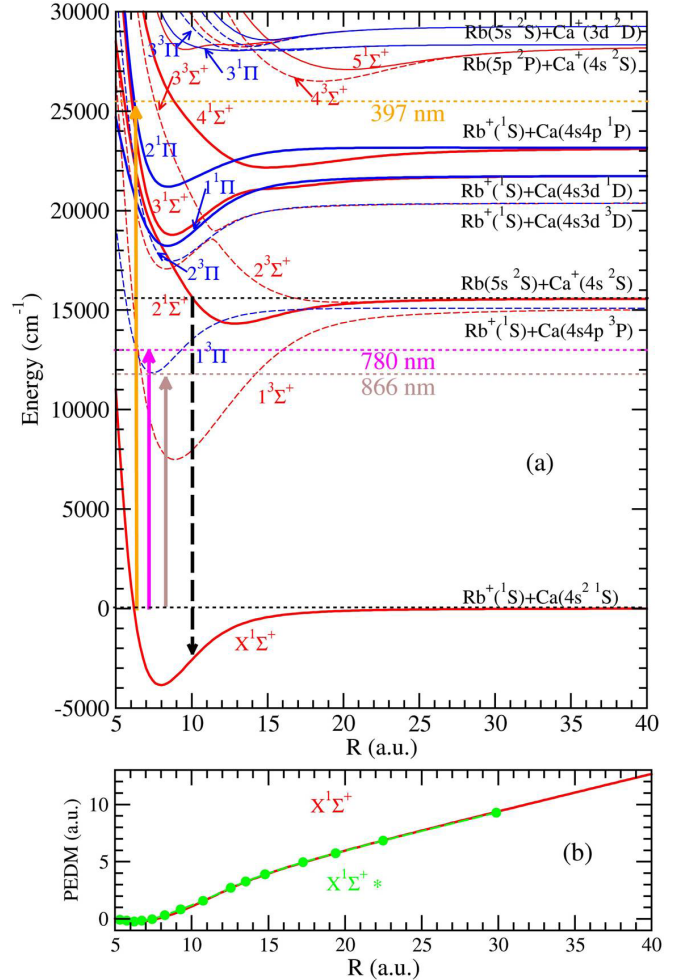

FIG. 2. (a) Hund's case *a* $RbCa^+$ PECs as functions of internuclear distance R. The origin of energies is taken at the asymptote of the electronic ground state $Rb^+(^1S) + Ca(4s^2\,^1S)$. The length of the vertical solid upward arrows represent the energies of the lasers present in the experiment [2] with wavelengths 397 nm (orange arrow), 780 nm (magenta arrow), and 866 nm (brown arrow). The black dashed downward arrow holds for the radiative association process (see the main text), resulting in the formation of $RbCa^+$ ions. (b) PEDM of the $X\,^1\Sigma^+$ state (solid red line) computed with the origin of distance taken at the $RbCa^+$ center of mass compared to the theoretical results of Ref. [29] (closed green dots).

the parametrization of the ECPs and CPPs is performed on the atomic energy spectrum of Rb and Ca^+. Inherently, the discrepancy for the $Rb^+(^1S) + Ca(4s^2\,^1S)$ limit can be larger than 100 cm^{-1} as the atomic energies of the neutral calcium atoms result from the FCI. Our results are in agreement with those of the recent investigation of Ref. [29] based on a very similar approach with, however, significant differences in the used parametrization. We note that for several asymptotes, our results are improved compared to Ref. [29].

Figure 2 displays the computed PECs for the $^1\Sigma^+, ^3\Sigma^+$, $^1\Pi$, and $^3\Pi$ electronic states up to the eighth dissociation limit. The corresponding spectroscopic constants are reported in the Appendix, showing an overall satisfactory agreement with Ref. [29]; a few differences are visible, however, which are discussed in the Appendix. There are two

noticeable patterns in Fig. 2. First, the $2\,^1\Sigma^+$ PEC correlated to $\mathrm{Rb}(5s\,^2S) + \mathrm{Ca}^+(4s\,^2S)$ (which is the entrance scattering channel in the experiment [2]) crosses the $1\,^3\Pi$ PEC dissociating into $\mathrm{Rb}^+(^1S) + \mathrm{Ca}(4s4p\,^3P)$ in two locations: $R_1 = 11.9$ a.u. and $R_2 = 17.4$ a.u. (1 a.u. $\equiv a_0 = 0.0529177210903$ nm). Then NRCE can occur, induced by SOC, as described in Ref. [27]. Second, the $6\,^1\Sigma^+$ and $5\,^3\Sigma^+$ PECs correlated to the $\mathrm{Rb}(5s\,^2S) + \mathrm{Ca}^+(3d\,^2D)$ limit, which is another possible entrance channel in the experiment as the metastable $3d\,^2D$ Ca$^+$ level is involved in the laser cooling cycle, exhibit an avoided crossing with the $5\,^1\Sigma^+$ and $4\,^3\Sigma^+$ PECs, respectively, in the $13a_0$–$15a_0$ range of internuclear distances (see the magnified figure in the Appendix). Therefore, excitation exchange toward the $\mathrm{Rb}(5p\,^2P) + \mathrm{Ca}^+(4s\,^2S)$ outgoing channel is expected, which will produce energetic Ca$^+(4s\,^2S)$ ions accompanied by radiative decay of the excited $\mathrm{Rb}(5p\,^2P)$ atom. For completeness, figures for selected PEDMs and TEDMs are reported in the Appendix, showing satisfactory agreement with Ref. [29].

To model the NRCE process, an accurate description of the R-dependent SOCs between the $2\,^1\Sigma^+$ and $1\,^3\Pi$ PECs is required, which results in their separation by an amount as small as 2 cm^{-1} at their crossing point around $17a_0$, according to Ref. [27]. Here, we used an alternative method to derive this coupling, and thus further assess the dependency of the NRCE cross section and rate with respect to the SOC amplitude (see Sec. V). The central idea is to involve only the atomic spin-orbit operators $H_{\mathrm{SO}}^i = \alpha_{\mathrm{SO}}^i \vec{\ell}_i \cdot \vec{s}_i$ and coupling constants α_{SO}^i ($i =$ A, B) for each of the A and B particles. The resulting matrix elements are easily evaluated when the particles are at large distances, considering a linear combination of atomic orbitals (LCAO) for the AB pair modeled as an effective two-electron system.

Our approach is based on the *quasidiabatic* method first presented in Ref. [36], which, to our knowledge, has been used only once for the NaCd van der Waals molecule [37]. It is described in detail in Ref. [26]. Briefly, we start with the Hund's case a diagonal Hamiltonian matrix $\mathbf{H}^0$, which contains the adiabatic Hund's case a PECs of Fig. 2 for each molecular symmetry $^{2S+1}\Lambda^p$, where S, Λ, p are the quantum numbers for the total electronic spin, the projection of the total electronic angular momentum on the molecular axis, and the parity for the symmetry with respect to a plane containing the molecular axis. Considering the N_{ref} eigenvectors associated to the N_{ref} lowest PECs for each symmetry at a large distance R_{ref} as a basis set representing the separated atoms, we apply a transformation, at every distance $R < R_{\mathrm{ref}}$, to the corresponding $N_{\mathrm{ref}} \times N_{\mathrm{ref}}$ diagonal matrix. It yields a quasidiabatic nondiagonal Hamiltonian matrix $\mathbf{H}_{\mathrm{diab}}(^{2S+1}\Lambda^p; R)$ which describes the initial adiabatic states in the basis set of the separated atoms. As depicted in Fig. 3, we assemble the $\mathbf{H}_{\mathrm{diab}}(^{2S+1}\Lambda^p; R)$ matrices for each symmetry involved in the spin-orbit interaction ($^3\Pi$, $^1\Pi$, $^3\Sigma^+$, for the Hund's case c symmetry $\Omega = 1$) into a single block-diagonal matrix $\mathbf{H}_{\mathrm{eff}}(\Omega^p; R)$. The blocks are connected through the atomic spin-orbit terms relevant for every atomic state (listed in Fig. 3), according the matrices displayed in the Appendix. Then two options are available:

(1) Diagonalizing $\mathbf{H}_{\mathrm{eff}}(\Omega^p; R)$ to obtain the adiabatic Hund's case c PECs for every Ω^p symmetry.
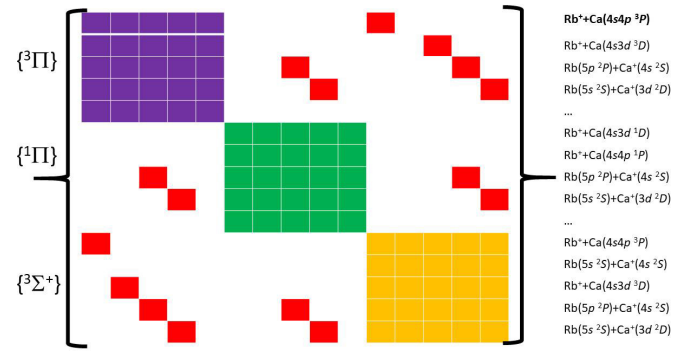

FIG. 3. A schematic representation of the effective Hamiltonian matrix $\mathbf{H}_{\mathrm{eff}}$, illustrated for the case of $\Omega = 1$. Three diagonal blocks (in purple, green, and orange) are present for the three relevant Hund's case a symmetries $^3\Pi$, $^1\Pi$, and $^3\Sigma^+$, respectively, while the atomic SOCs (red squares) are connecting states from different blocks correlated with the same dissociation limit (thus the same fine-structure manifold).
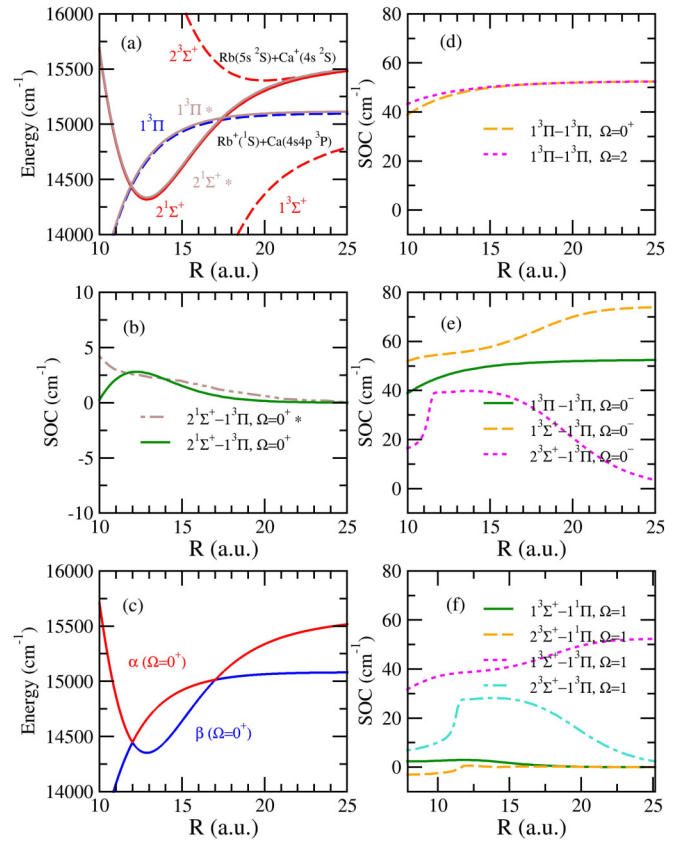

FIG. 4. (a) Magnified view of the RbCa$^+$ PECs involved in the NRCE process $\mathrm{Rb}(5s\,^2S) + \mathrm{Ca}^+(4s\,^2S) \rightarrow \mathrm{Rb}^+ + \mathrm{Ca}(4s4p\,^3P)$. The theoretical results from Ref. [27] are labeled by a star $*$ (brown line). (b) SOC between the $2\,^1\Sigma^+$ and the $1\,^3\Pi$ states computed in the present work for the $\Omega = 0^+$ symmetry, together with the one computed in Ref. [27] (labeled with a star $*$, dashed brown line). (c) Adiabatic PECs resulting from the diagonalization of the $\mathbf{H}_{\mathrm{eff}}(\Omega^p; R)$ matrix (see the main text). (d) Diagonal SOC for the $\Omega = 0^+$, 2 symmetries. (e) SOCs for the $\Omega = 0^-$ symmetry. (f) SOCs for $\Omega = 1$ symmetry. Note that the kinks in the coupling between $2\,^3\Sigma^+$ and $1\,^3\Pi$ visible in (e) and (f) are due to the avoided crossing around 12 a.u. of the $2\,^3\Sigma^+$ and $3\,^3\Sigma^+$ PECs (see Fig. 2.)

(2) Performing the inverse transformation on $\mathbf{H}_{\text{eff}}(\Omega^p; R)$ back to the original adiabatic basis, leading to a matrix $\mathcal{H}_0(R)(\Omega^p; R)$ with diagonal and off-diagonal matrix elements for the molecular SOCs between the involved molecular symmetries.

Following Ref. [26], we selected $N_{\text{ref}} = 40$ Hund's case *a* states in each molecular symmetry and we optimized the transformation to have the quasidiabatic matrix elements converged for the eight lowest reference states.

Figure 4 displays the Hund's case *a* PECs [Fig. 4(a)] relevant for the NRCE process $\text{Rb}(5s\,^2S) + \text{Ca}^+(4s\,^2S) \rightarrow \text{Rb}^+ + \text{Ca}(4s4p\,^3P)$, the associated SOCs extracted from the diagonal and off-diagonal matrix elements of $\mathcal{H}_0(R)(\Omega^p; R)$ [Figs. 4(b) and 4(d)–4(f)], and the eigenvalues of $\mathbf{H}_{\text{eff}}(\Omega^p; R)$ [Fig. 4(c)]. The $\text{Rb}^+ + \text{Ca}(4s4p\,^3P)$ asymptote is now split into three components $\text{Rb}^+ + \text{Ca}(4s4p\,^3P_{0,1,2})$, and the weakly R-dependent SOCs between the corresponding molecular states reflect the magnitude of the SO splitting of atomic $\text{Ca}(4s4p\,^3P)$. As their PECs are correlated to different asymptotes, the SOC $W_{\text{SO}}(R)$ between the $^1\Sigma^+$ and $^3\Pi$ crossing states [Fig. 4(b), $\Omega = 0^+$], is weak at their crossing points $(W_{\text{SO}}(R_1 = 11.9a_0) = 2.77$ cm^{-1}, and $W_{\text{SO}}(R_2 = 17.4a_0) = 0.52$ cm^{-1}). This result is in good agreement with the pub-

lished determination from Ref. [27] in this region, as well as the PECs themselves [Fig. 4(a)].

III. RADIATIVE ASSOCIATION OF RbCa$^+$ AND BLACKBODY RADIATION

The RA process was studied in paper I for a series of ionic molecular species composed of Rb and alkaline-earth ions, including RbCa$^+$. It is illustrated by the dashed black arrow in Fig. 2, namely, the spontaneous emission of a photon during the collision between cold ground-state Rb atoms and Ca$^+$ ions at a relative energy E_{coll} via the $2\,^1\Sigma^+$ state toward the $X\,^1\Sigma^+$ state with a typical (constant) rate coefficient of about 10^{-5} the Langevin rate, namely $\simeq 3 \times 10^{-14}$ cm^{3}s^{-1}. Assuming an averaged density of Rb atoms in the MOT of 10^9 cm^{-3} [2], the RA rate has a magnitude of about 10^{-5} s^{-1}.

The population distribution over the rovibrational levels $|v'_f, J'_f\rangle$ of the RbCa$^+$ $X\,^1\Sigma^+$ ground state (the f channel), starting from the entrance channel i with a collision energy E_{coll} and a rotational state (or partial wave) J_i (thus $J_f = J_i \pm 1$), is described as the fraction $F(v'_f, J'_f, E_{\text{coll}}, J_i)$ of the total population of the RbCa$^+$ bound levels induced by RA,

$$F(v'_f, J'_f, E_{\text{coll}}, J_i) = \frac{\omega_{v'_f, J'_f, E_{\text{coll}}, J_i}|\langle X\,^1\Sigma^+, v'_f, J'_f|D_{fi}(R)|2\,^1\Sigma^+, E_{\text{coll}}, J_i\rangle|^2}{\sum_{v'_f=0}^{v'_{\max}} \omega_{v'_f, J'_f, E_{\text{coll}}, J_i}|\langle X\,^1\Sigma^+, v'_f, J'_f|D_{fi}(R)|2\,^1\Sigma^+, E_{\text{coll}}, J_i\rangle|^2}, \tag{1}$$

where the energy difference between the corresponding two levels is $\hbar\omega_{v'_f, J'_f, E_{\text{coll}}, J_i}$. The R-dependent TEDM $D_{fi}(R)$ between the $X\,^1\Sigma^+$ and the $2\,^1\Sigma^+$ states was given in paper I. The ket $|E_{\text{coll}}, J_i>$ represents the energy-normalized radial continuum wave function which describes the two colliding particles in the $2\,^1\Sigma^+$ entrance channel. The summation is performed up to the uppermost calculated $X\,^1\Sigma^+$ vibrational level $v'_{\max} = 141$.

In the experiments [2,4], the kinetic energy of the collision is determined by that of the Ca$^+$ ion, which could span a range of equivalent temperatures up to a few Kelvin. In Fig. 5, we display the distribution of Eq. (1) for $J_i = 0$, $J_f = 1$ and for different values of colliding energies ϵ_i corresponding to temperatures $E_{\text{coll}}/k_B = 2.4$ μK, 5.8 mK, and 2.8 K. The distribution is independent of the temperature and obviously consistent with the results of paper I at 100 μK, and those of Ref. [29] at 1 μK. In particular, we find that the RbCa$^+$ molecular ions are preferably formed in deeply bound vibrational levels with a maximum fraction centered at $v_f = 21$. More importantly, 96% of the formed molecular ions are mainly distributed in $v_f = 16 - 60$, and the deeper bound levels $v_f \leqslant 15$ are unlikely to be populated by RA.

Another feature of the experiment is that the formed ground-state RbCa$^+$ ions reside quite a long time ($\approx$ minutes) in the trap, so in principle their vibrational population could be rearranged due to the influence of BBR at room temperature (say, 300 K). The BBR energy density $\rho(\omega)$ for a given frequency ω in atomic units ($\hbar = e = m_e = 1$) (see, for instance,

Ref. [38]) is given by

$$\rho(\omega) = \frac{2\omega^3}{\pi c^3} N(\omega) \equiv \frac{2\omega^3}{\pi c^3} \frac{1}{\exp\left(\frac{\omega}{k_B T}\right) - 1}, \tag{2}$$
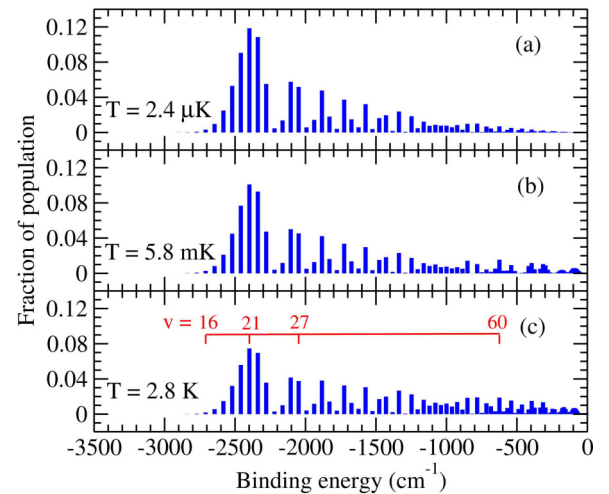

FIG. 5. Fraction of population (by RA from the $2\,^1\Sigma^+$ entrance channel) of the RbCa$^+$ ground-state vibrational levels [displayed in red in panel (c)] as a function of their binding energy for three selected collision energies (a) $E_{\text{coll}}/k_B = 2.4$ μK, (b) $E_{\text{coll}}/k_B = 5.8$ mK, and (c) $E_{\text{coll}}/k_B = 2.8$ K.
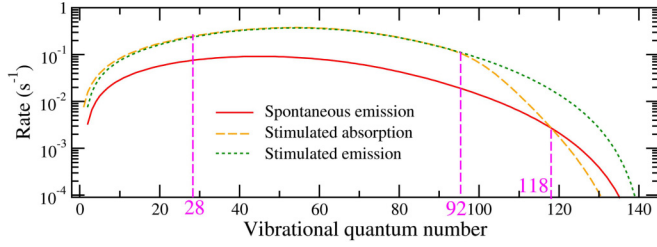
FIG. 6. Rates for spontaneous (stimulated) emission and absorption of the vibrational levels of the RbCa$^+$ $X^1\Sigma^+$ ground state. The stimulated radiation rate is the sum of the absorption and stimulated emission rates. The vertical dashed line at $v = 28$ marks the photodissociation threshold for the 397 nm laser (see Sec. IV). At $v = 92$, the absorption rate becomes smaller than the stimulated emission rate, and than the spontaneous emission rate at $v = 118$.

where $N(\omega)$ stands for the number of BBR photons. Assuming that a vibrational level v_i (with binding energy ϵ_{v_i}, assuming a rotational state $J_i = 0$) of the RbCa$^+$ ground state is exposed to BBR, transitions toward other ground-state vibrational levels v_f (with binding energy ϵ_{v_f}, assuming $J_f = 0$) can occur. The inverse of the resulting lifetime τ_{v_i} of the v_i level can be expressed as

$$\tau_{v_i}^{-1} = \sum_{\epsilon_{v_f} < \epsilon_{v_i}} \Gamma^{\mathrm{SpE}} + \sum_{\epsilon_{v_f} < \epsilon_{v_i}} \Gamma^{\mathrm{StE}} + \sum_{\epsilon_{v_i} < \epsilon_{v_f}} \Gamma^{\mathrm{Abs}}, \quad (3)$$

where Γ^{SpE}, Γ^{StE}, and Γ^{Abs} are the rates for spontaneous emission, stimulated emission, and absorption, respectively. Defining $\omega_{fi} = |\epsilon_{v_f} - \epsilon_{v_i}|$, we have

$$\Gamma^{\mathrm{SpE}} = \frac{4\omega_{fi}^3}{3c^3} |\langle v_f, J_f = 1|D_X(R)|v_i, J_i = 0\rangle|^2 \quad (4)$$

and

$$\Gamma^{\mathrm{StE}} \equiv \Gamma^{\mathrm{Abs}} = \Gamma^{\mathrm{SpE}} N(\omega). \quad (5)$$

where $D_X(R)$ is the R-dependent PEDM in the ground state of RbCa$^+$ [Fig. 2(b)].

The calculated rates for spontaneous emission, stimulated emission, and absorption are displayed in Fig. 6. The former process is significantly less efficient than the stimulated ones but, by comparison, are larger than the RA rate. In other words, once a molecular ion is created by RA in the range of vibrational levels [16–60] (Fig. 5), it will be sensitive to this class of processes. However, the modification of the vibrational distribution is likely to be minimal, as suggested by Fig. 7: the transitions induced by BBR almost exclusively occur toward the next vibrational level (i.e., $v_f - v_i = \pm 1$), while the absorption and the stimulated emission rates are very similar to each other.

IV. PHOTODISSOCIATION OF RbCa$^+$ CREATED BY RADIATIVE ASSOCIATION

One of the main features of the hybrid-trap experiments is that several lasers are involved and switched on during the measurements. Therefore, the created molecular ions are likely to be exposed to strong PD, as previously emphasized for Rb$_2^+$ ions [23] and RbBa$^+$ ions [7], while in some-
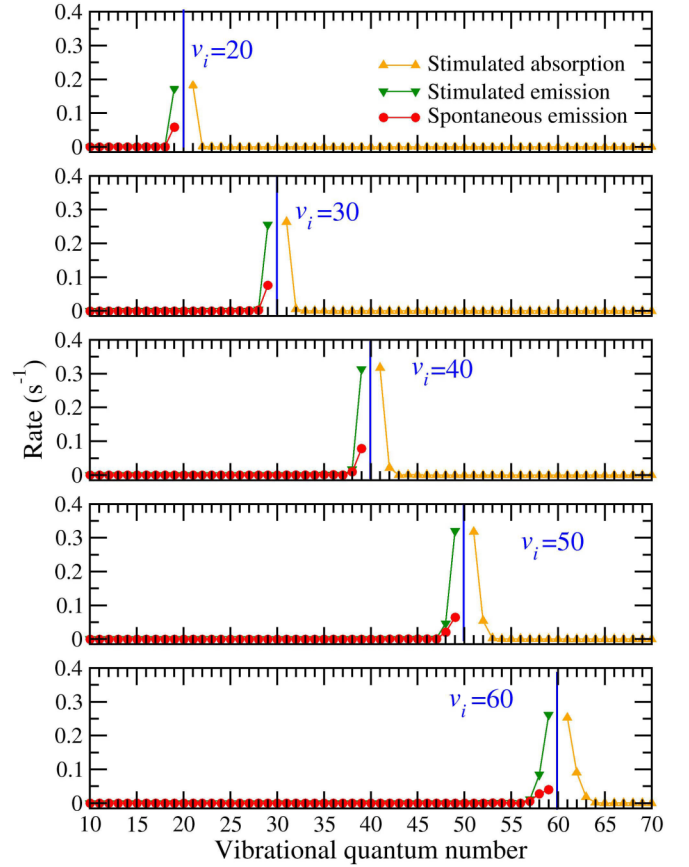

FIG. 7. Rates for spontaneous (stimulated) emission and absorption for the $X^1\Sigma^+$ ground state vibrational levels $v_i = 20, 30, 40, 50, 60$ toward every $X^1\Sigma^+$ final level v_f for $J_i = 0 \rightarrow J_f = 1$.

what different experimental conditions. In the experiments of Refs. [2,4] three cooling lasers are present (Fig. 2) with the following wavelengths: 397 nm and 866 nm for the $4s\,^2S_{1/2} \rightarrow 4p\,^2P_{1/2}$ cooling transition and the $3d\,^2D_{3/2} \rightarrow 4p\,^2P_{1/2}$ repumping transition in Ca$^+$, respectively, and 780 nm for $5s\,^2S_{1/2} \rightarrow 5p\,^2P_{3/2}$ cooling transition in ^{87}Rb. We see in Fig. 2 that only the laser at 397 nm is expected to photodissociate ground-state RbCa$^+$ ions. Indeed, due to the selection rules for dipolar transitions, only dissociation channels associated with the continuum region of $^1\Sigma^+$ and $^1\Pi$ states can be reached from the ground electronic state. The energies of 780 nm and 866 nm photons are too low to induce photodissociation, even from a weakly bound, i.e., vibrationally highly excited, RbCa$^+$ molecular ion in its electronic ground state. The 397 nm laser is the only one which can dissociate ground-state RbCa$^+$ leading to five possible exit channels.

Our analysis is performed considering Hund's case a PECs, neglecting SOCs which are rather small compared to the photon energies, so they should not significantly affect the results. We calculate the PD rate of a RbCa$^+$ ground-state molecular ion created in a rovibrational level v_i, J_i, considering all the excited molecular states f that are energetically open with the above lasers. The final continuum state is labeled by ϵ_f, J_f, where ϵ_f is the relative kinetic energy of the dissociated
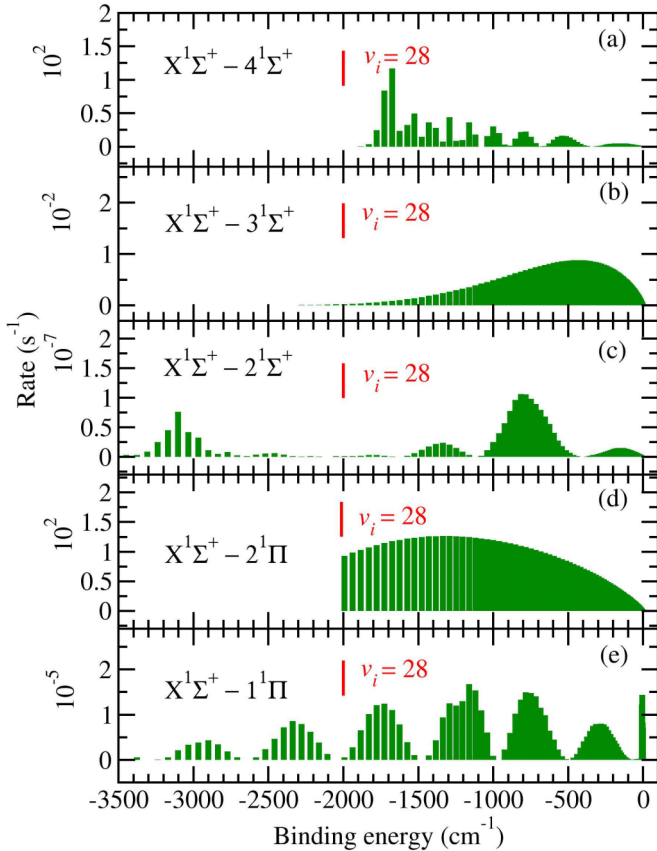
FIG. 8. Calculated photodissociation rates induced by the 397 nm cooling laser, assuming a laser intensity of $I = 400$ mW/cm^2, as functions of the binding energy E_{v_i} of the $X\,^1\Sigma^+$ vibrational levels v_i, for the five open exit channels (a) $4\,^1\Sigma^+$, (b) $3\,^1\Sigma^+$, (c) $2\,^1\Sigma^+$, (d) $2\,^1\Pi$, and (e) $1\,^1\Pi$. The photodissociation threshold $v_i = 28$ is specified in red.

atom-ion pair above the dissociation energy of the f state. The PD rate is given by

$$
\begin{aligned}
&\Gamma_{\mathrm{PD}}(v_i, J_i, \epsilon_f, J_f) \\
&= \sigma_{\mathrm{PD}}(v_i, J_i, \epsilon_f, J_f) K \\
&= S_{J_i, J_f} \frac{4\pi^2 a_0^2}{3\hbar c} E_\lambda | < \epsilon_f, J_f |D_{fi}(R)|v_i, J_i > |^2 \frac{I}{\hbar\omega_\lambda}, \quad (6)
\end{aligned}
$$

where σ_{PD} is the state-to-state dissociation cross section, K is the flux of dissociating light with intensity I, and $E_\lambda = hc/\lambda \equiv \hbar\omega_\lambda$ is the photon energy with wavelength λ and angular frequency ω. The final energy $\epsilon_f = E_\lambda - |E_i - E_f| - |E_{v_i, J_i}|$ is obtained from the difference of energies of the dissociation limits of the initial (E_i) and final (E_f) channels, and from the binding energy E_{v_i, J_i} of the initial level (v_i, J_i). The Hönl-London factors S_{J_i, J_f} are also included. We note, however, that according to Ref. [7], the total PD cross section is independent of J_i when it is summed over the contributions of the P ($J_f = J_i - 1$), Q ($J_f = J_i$) and R ($J_f = J_i + 1$) branches. Therefore, we assume $J_i = 0$ in the following, for the sake of simplicity.

The corresponding PD rates for a laser intensity of $I = 400$ mW/cm^2 [4] are represented in Fig. 8 as a function of the binding energy E_{v_i} of the initial ground-state level. Two chan-

nels, $4\,^1\Sigma^+$ and $2\,^1\Pi$, are reached with a significant rate compared to the others: this is expected from the matching in distance of the repulsive branch of their PECs with the extension of the ground-state potential well for the energy of the 397 nm laser. We also see that, due to the large energy difference between the ground-state PEC and the final ones, vibrational levels below $v_i = 28$ cannot be photodissociated. According to the definition of the final energy ϵ_f given above, only ground-state ions created in $v \geqslant 28$ can undergo PD with $\epsilon_f > 0$. From the vibrational populations created by RA reported in Sec. III, we infer that about 41% of the molecular ions with $v_i > 28$ would be dissociated by the 397 nm laser, while about 59% of the molecular ions created in levels below $v_i = 28$ are protected against PD, and thus could be detected, in agreement with the experimental observations of Refs. [2,4].

V. NONRADIATIVE CHARGE EXCHANGE BETWEEN GROUND STATE Rb AND Ca$^+$

A previous quantum-scattering study of the NRCE between ground-state Ca$^+$ and Rb has already been reported in Refs. [27,28]. As our molecular data, namely, the PECs and SOCs, are noticeably different from the ones of these references, we recalculate the corresponding rates in order to evaluate their sensitivity. As recalled in Sec. II, the NRCE process involves the $2\,^1\Sigma^+$ (entrance channel) and the $1\,^3\Pi$ PECs (outgoing channel), which cross each other in two locations, $R_1 = 11.9a_0$ and $R_2 = 17.4a_0$ [Fig. 4(a)]. In Hund's case c, the former state gives rise to a single state with $\Omega = 0^+$, and the latter to four states with $\Omega = 0^+, 0^-, 1, 2$, correlated with the dissociation limits Rb$^+$(^1S)+Ca($4s4p\,^3P_j$), with $j = 0, 1, 2$. The corresponding spin-orbit Hamiltonian matrices are presented in the Appendix and involve the R-dependent SOCs computed in Sec. II and displayed in Figs. 4(b) and 4(d)–4(f).

Thus, only the $\Omega = 0^+$ symmetry is relevant for NRCE through the 2×2 SO matrix reported in the Appendix. The SOC between the $2\,^1\Sigma^+$ and $1\,^3\Pi$ states [Fig. 4(b)] vanishes at large distances as their PECs are correlated with different dissociation limits. It smoothly increases in the crossing region due to the configuration mixing as the internuclear distance R decreases. The SOC diagonal term for $1\,^3\Pi$ [Fig. 4(d)] has a finite value at large distances, corresponding to the SO splitting of the Ca atom (see Appendix), and smoothly decreases with decreasing R due to this configuration mixing, too. Following Refs. [27,28], we do not consider any rotational coupling between the $2\,^1\Sigma^+$ and $1\,^3\Pi$ states as they have different spin multiplicity, so the rotational quantum number (or the partial wave) noted ℓ in this section is assumed to be conserved during the NRCE.

The $\Omega = 0^+$ PECs obtained after diagonalization of the 2×2 SO matrix are drawn in Fig. 9, together with a magnification of the region of the crossings. Two rather small avoided crossings are visible, slightly shifted compared to the location of the crossing between Hund's case a PECs, due to the energy shift of the $1\,^3\Pi$ dissociation limit equal to $A_{sp}/3 \equiv [E(^3P_2) - E(^3P_0)]/3$ (see the Appendix), which is induced by the diagonal term of the SOC matrix. These avoided crossings
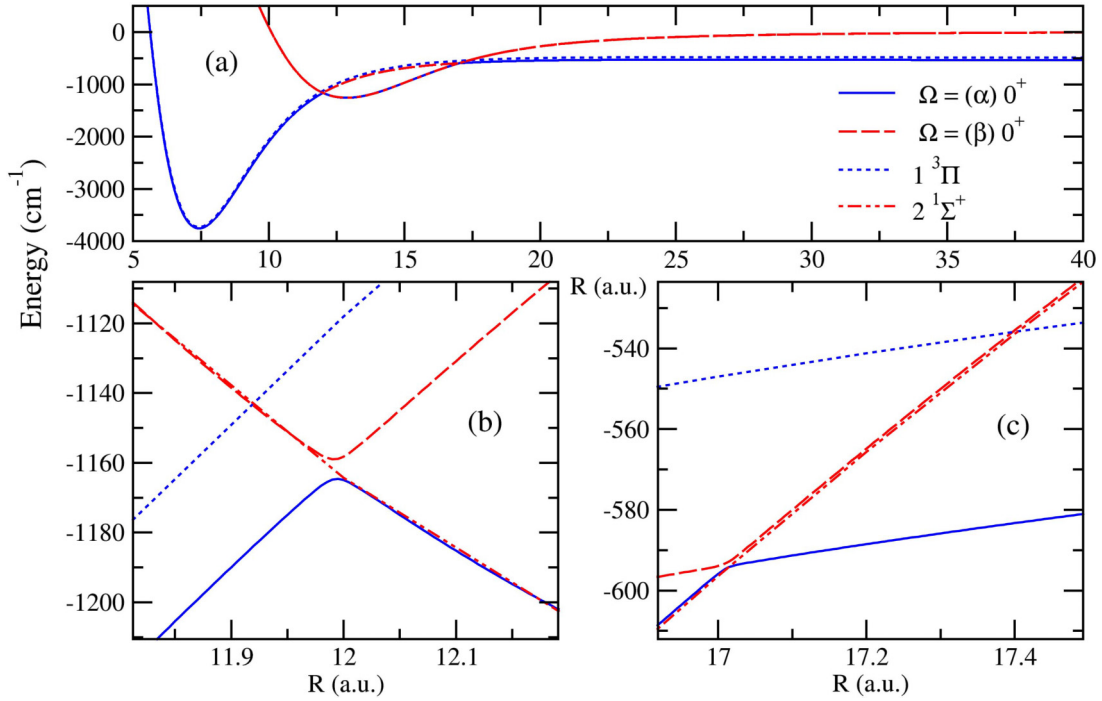
FIG. 9. (a) RbCa$^+$ Hund's case a $2\,^1\Sigma^+$ and $1\,^3\Pi$ PECs and Hund's case c PECs labeled by (α) and (β) for $\Omega = 0^+$, (b) magnification around the crossing regions at $R_1 = 11.9a_0$, and (c) at $R_2 = 17.4a_0$.

are expected to bring prominent contributions to the NRCE [27,28].

To precisely account for the contributions of these two avoided crossings, we solve the set of Schrödinger equations for the two electronic states coupled by the SO interaction, for each ℓ, using the standard log-derivative propagator [39], yielding the usual scattering matrix **S**. The cross section for the NRCE process is determined at each relative collision energy $E_{coll} = \mu v_{coll}^2/2$ (with v_{coll} the relative velocity) by the off-diagonal elements S_{if} of the **S** matrix, and expressed as a sum over partial waves ℓ,

$$\sigma_{NRCE}(E_{coll}) = p\frac{\pi\hbar^2}{2\mu E_{coll}}\sum_{\ell=0}^{\infty}(2\ell+1)|S_{if}|^2, \quad (7)$$

where $p = 1/4$ is the statistical weight for the population of the $X\,^1\Sigma^+$ state from the entrance channel and μ is the reduced mass of RbCa$^+$. We find that the transition probability $|S_{if}|^2$ of the NRCE is equal to 0.006 for $\ell = 0$ at low collision temperatures, which is consistent with the result of 0.007 of Ref. [27]. This is a first sign that the differences in the PECs and SOCs between our paper and those of Ref. [27] do not significantly influence the probability. The NRCE cross section is converged for every energy with respect to a maximum number of partial waves, from 5 at $T = E_{coll}/k_B = 10^{-6}$ K up to 122 at $T = E_{coll}/k_B = 10$ K. The results are displayed in Fig. 10(a), as functions of the collision energy E. The cross sections exhibit the expected $E_{coll}^{-1/2}$ slope of the Langevin model and numerous shape resonances in the entrance channel.

It is worthwhile noticing that just like the resonant scattering processes (charge exchange, spin exchange) involving two interfering channels with the same asymptotic energy [20,40–42], a clear manifestation of the so-called phase-locking is visible in the case of the present *nonresonant* CE process (Fig. 11): the transition probability remains constant, equal
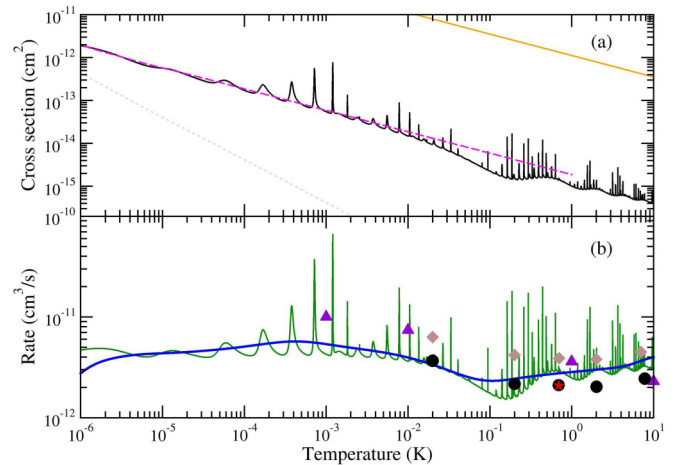

FIG. 10. (a) Computed cross section (solid black curve) for the NRCE process Rb($5s\,^2S$)+Ca$^+$($4s\,^2S$) $\rightarrow$ Rb$^+$(^1S) + Ca($4s4p\,^3P$) as a function of the temperature $T = E_{coll}/k_B$ related to the relative collision energy E_{coll} compared to the Langevin cross section (solid orange line) and to the expression of Eq. (9) (first term: dotted grey line; second term: dashed magenta line). (b) Nonthermalized (solid green oscillatory line) and Boltzmann-thermalized (superimposed solid blue line) NRCE rate coefficients compared to the theoretical results of Ref. [27] averaged with a Boltzmann distribution (violet triangles), with the distribution determined by the ion velocities (brown diamonds, see Fig. 5(c) of Ref. [5]), to the down-scaled experimental data (black circles) of Ref. [4] (see text), and to the experimental value at 2 K of Ref. [4] (red star).
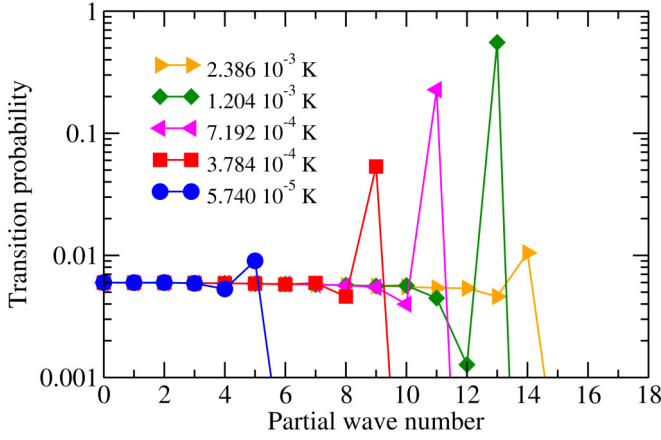
FIG. 11. Computed NRCE probability as a function of the partial wave ℓ for selected temperatures $T = E_{coll}/k_B$ where a shape resonance (the peak on each curve) occurs.

to the one of the s-wave, for many partial waves at a given energy and over a broad range of energies. This is due to the small energy difference between the two asymptotes $Rb(5s\,^2S) + Ca^+(4s\,^2S)$ and $Rb^+(^1S) + Ca(4s4p\,^3P)$ (see the Appendix) compared to the well depth of the relevant PECs (see the Appendix). Therefore, this pattern is also relevant for quasiresonant processes. Recasting Eq. (7) as

$$\sigma_{NRCE}(E_{coll}) = p \frac{\pi}{2\mu E_{coll}} \sum_{\ell=0}^{\infty} (2\ell + 1) \sin^2 \left(\delta_\ell^i - \delta_\ell^f \right), \quad (8)$$

where δ_ℓ^i (δ_ℓ^f) is the phase shift for the i or $2\,^1\Sigma^+$ (f or $1\,^3\Pi$), channel, we see that the phase shift difference $\Delta\delta_\ell = \delta_\ell^i - \delta_\ell^f$ is almost ℓ independent, and we can determine $\sin^2 \Delta\delta_\ell$ from our results at $\ell = 0$. In Ref. [41], such an approximation was named an s-wave signature and the cross section at energy
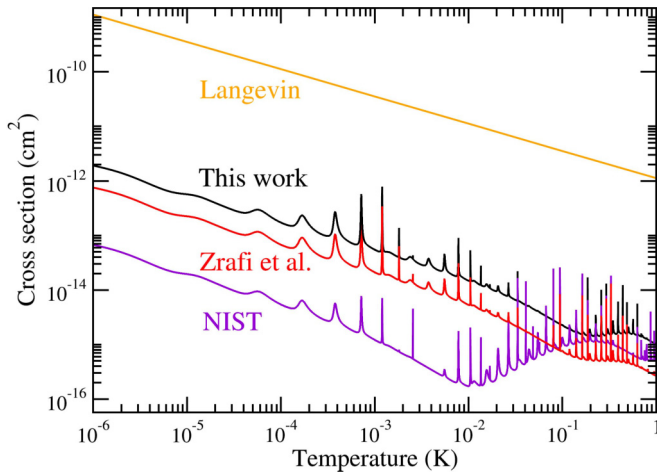

FIG. 12. NRCE cross sections obtained after the shift of the energy D_f of the dissociation limit of the exit channel $1\,^3\Pi$ PEC to D_f(NIST) (violet) and to D_f ([29]) (red) compared to the present value (black). The Langevin cross section σ_L (orange) is plotted for comparison.

E_{coll} is expressed as

$$\sigma_{NRCE}(E_{coll}) = p \left(\frac{\pi}{2\mu E_{coll}} + \sigma_L(E_{coll}) \right) \sin^2 \Delta\delta_0(E_{coll}), \quad (9)$$

where $\Delta\delta_0(E_{coll})$ is the s-wave phase shift depending on the collision energy E_{coll}, and $\sigma_L(E_{coll})$ the Langevin cross section, which is then rescaled with the $\sin^2 \Delta\delta_0(E_{coll})$ factor. We see in Fig. 10 that Eq. (9) reproduces the energy variation of the baseline of the cross section obtained by the full quantum scattering calculation.

The nonthermalized rate coefficient is $K_{NRCE}(E_{coll}) = \sigma_{NRCE}(E_{coll}) \times v_{coll}$, with v_{coll} the relative velocity. While the ion velocity distribution is far from following a Maxwell-Boltzmann distribution [5], we nevertheless calculate a rate coefficient convoluted with a Maxwell-Boltzmann distribution of the relative velocities v_{coll} of the particle pairs at temperature T for the purpose of comparison:

$$K_{NRCE}(T) = \frac{2}{\sqrt{\pi}(k_B T)^{3/2}} \int_0^{\infty} K_{NRCE}(E_{coll})$$
$$\times \sqrt{E_{coll}} e^{-E_{coll}/k_B T} dE_{coll}. \quad (10)$$

The nonthermalized rate is found approximately constant (around 5×10^{-11} cm^{3}s^{-1}) due to the previously observed $E_{coll}^{-1/2}$ slope of the cross section [Fig. 10(b)]. All shape resonances are smoothed out after the thermal average, as they are much narrower than the velocity distribution. Our results are consistent within a factor of 2 with the theoretical values of Ref. [28]. The differences between our model and Ref. [28] are commented on further in the Appendix. At this stage, we can say that despite their differences, both models provide results consistent within a factor of ≈ 2 with the experimental results at 2 K reported in Ref. [5] or with the measured channel-averaged rate constants in Fig. 6(a) of Ref. [5], assuming a downscaling by a factor $(1/6) \times (3/4)$ to account for the contribution of the charge exchange resulting from the lowest collision channel (see more details in the Appendix).

Due to the above s-wave signature effect, the issue of the precision of the theoretical model should be taken with great care. For instance, in the present case, we note in the Appendix that the dissociation energy D_f of the exit charge-exchange channel $Rb^+ + Ca(4s4p\,^3P)$ is not properly determined compared to the sum of the atomic values extracted from the NIST database [43]. We thus performed two additional calculations of $\sigma_{NRCE}(E_{coll})$, keeping the same entrance channel and SOC, and vertically shifting the $1\,^3\Pi$ PEC downward to D_f(NIST) or upward to D_f ([29]). As expected, Fig. 12 shows differences larger than one order of magnitude in the s-wave regime due to the strong variation of the phase difference between the channels, while the cross section spreads over a factor of ≈ 5 in the Kelvin range.

VI. CONCLUSION

We theoretically investigated the collisional dynamics of laser-cooled Rb atoms and Ca$^+$ ions in the context of the hybrid trap experiment of Refs. [2,3]. We demonstrated that cold RbCa$^+$ ground-state molecular ions are created by RA and that they are protected against PD, provoked by BBR and by the Ca$^+$ cooling laser at 397 nm. This study yields
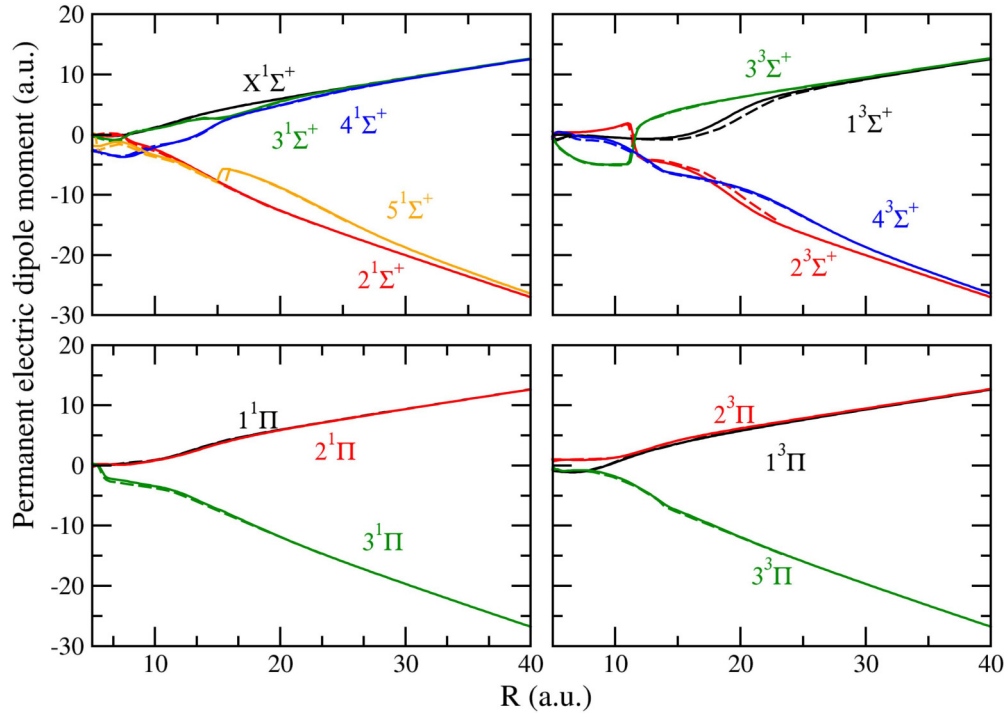
FIG. 13. Selected PEDMs computed in this paper (solid lines) compared to Ref. [29] (dashed lines).

a consistent interpretation of the direct observation of RbCa$^+$ ions in the experiments [2,5], in contrast with other hybrid trap experiments using other species (see, for instance, Ref. [7]). Based on updated molecular data, we also confirm that the NRCE, induced by spin-orbit interaction, is a dominant loss process and obtains rates in agreement with experimental observations and a previous calculation [5,28]. Our work also emphasizes the extreme sensitivity of the model to the accuracy of the molecular data (PECs, SOCs). An analogous full quantum scattering treatment including SOCs performed in the laboratory frame is currently in progress for RbSr$^+$ and LiBa$^+$ following the recent experimental results of Ref. [46].

APPENDIX

1. Molecular data

The parameters used are updated from our previous publications [30,31]. The optimized basis set for Ca$^+$ is composed of a large set of Gaussian orbitals ($9s$, $8p$, $8d$, $2f$). The cutoff parameters of the core-polarization potential are, in atomic units, ($\rho_s^{Ca^+} = 1.89095$, $\rho_p^{Ca^+} = 1.6528$, $\rho_d^{Ca^+} = 1.827734$), and the ionic core polarizability is $\alpha^{Ca^{2+}} = 3.522a_0^3$ [44].

The basis set of Rb is extended with an additional Gaussian f-orbital compared to Ref. [30]. Under such conditions,
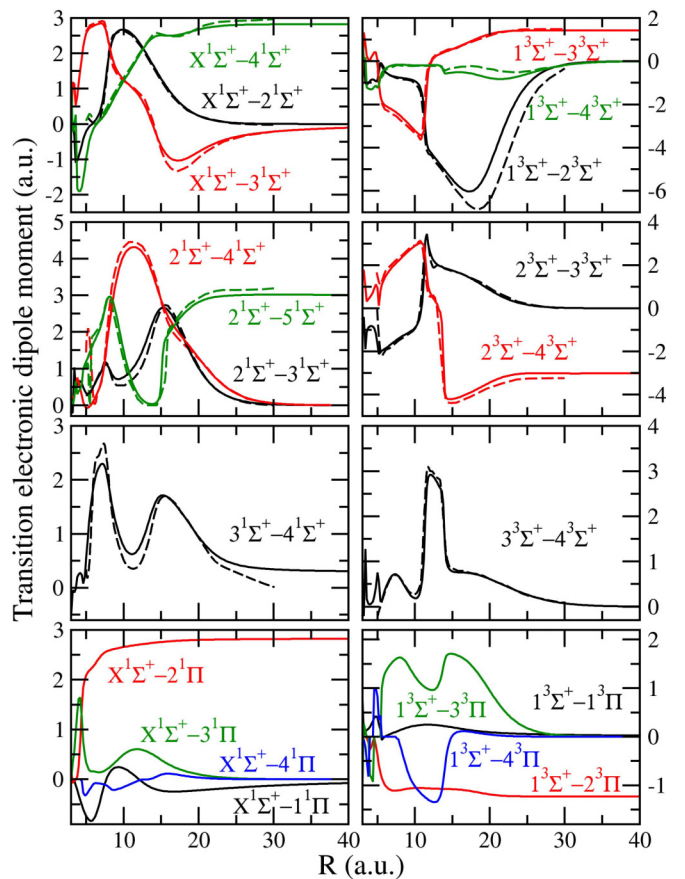

FIG. 14. Selected TEDMs computed in this paper (solid lines) compared to Ref. [29] (dashed lines).
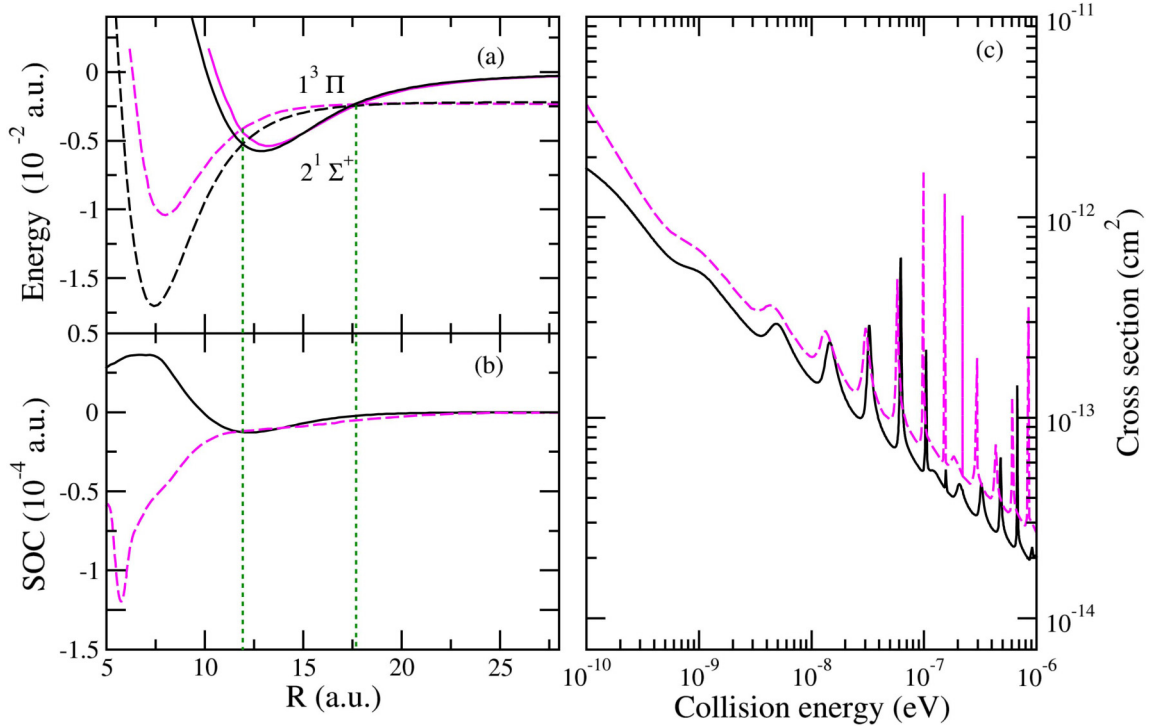
FIG. 15. This work (black) and Ref. [28] (magenta): (a) Hund' case *a* PECs of the $1\,^3\Pi$ (dashed line) and $2\,^1\Sigma^+$ (solid line) states, the vertical dashed lines indicate the two crossings; (b) SOC between the $1\,^3\Pi$ and $2\,^1\Sigma^+$ states, the vertical dashed lines mark the values of SOC at the two crossings; (c) The calculated NRCE cross sections as a function of the collision energy.

we calculated the energies for the dissociation limits of the RbCa$^+$ PECs, which are compared to other values in Table I. We see that our basis choice significantly improves the quality of the energy of several atomic states in comparison to Ref. [29]. Numerous PECs have been calculated, for which we report selected spectroscopic constants in Table II, which are compared to the results from Ref. [29]: Results for the equilibrium distance are in very good agreement, while we found values for the harmonic constant ω_e larger by about 0.5–1 cm^{-1} than those in Ref. [29]. The differences in the excitation energy T_e reflect those reported in the dissociation limits. The well depths D_e are in agreement within ≈ 100 cm^{-1} between the two calculations, corresponding to the typical

precision of such calculations. Nevertheless, Figs. 13 and 14 display our results for permanent and transition electric dipole moments, which are quantities sensitive to the structure of the electronic wave functions: we see that the agreement with Ref. [29] is very satisfactory, confirming that both calculations are very similar.

2. Spin-orbit coupling matrices

To describe SOC in the Rb$^+$ + Ca($4s4p\,^3P$) limit, the Hund's case *c* quantum number $|\Omega|$ can assume the values $0^+, 0^-, 1$. The total potential energy matrices of Rb($5s\,^2S$)

TABLE I. Energy of the dissociation limits of RbCa$^+$ PECs with respect to an origin taken at Rb$^+$+Ca^{2+}. The energy differences δE are calculated as $\delta E = E(\text{NIST}) - E$ (this paper) and $\delta E = E(\text{NIST}) - E$ [29].

	Theory (cm^{-1})		NIST (cm^{-1})	δE (cm^{-1})	
Asymptote	This paper	[29]	[43]	This paper	[29]
Rb$^+$(^1S) + Ca($4s^2\,^1S$)	$-145\,026$	$-144\,904$	$-145\,058$	-32	-154
Rb$^+$(^1S) + Ca($4s4p\,^3P$)	$-129\,950$	$-129\,624$	$-129\,795$	155	-171
Rb($5s\,^2S$) + Ca$^+$($4s\,^2S$)	$-129\,444$	$-129\,445$	$-129\,443$	1	2
Rb$^+$(^1S) + Ca($4s3d\,^3D$)	$-124\,644$	$-124\,136$	$-124\,702$	-58	-566
Rb$^+$(^1S) + Ca($4s3d\,^1D$)	$-123\,274$	$-122\,611$	$-123\,208$	66	-597
Rb$^+$(^1S) + Ca($4s4p\,^1P$)	$-121\,878$	-121574	$-121\,405$	473	169
Rb($5p\,^2P$) + Ca$^+$($4s\,^2S$)	$-116\,707$	$-116\,724$	$-116\,705$	2	19
Rb($5s\,^2S$) + Ca$^+$($3d\,^2D$)	$-115\,757$		$-115\,756$	1	

TABLE II. Computed spectroscopic constants of RbCa$^+$. Equilibrium interatomic distances R_e, well depths D_e, transition energies T_e, harmonic constants ω_e, anharmonic vibrational frequencies $\omega_e \chi_e$, and rotational constants B_e. Note that the T_e value for the $1\,^3\Pi$ PEC marked with a $*$ symbol is taken from Ref. [29], where it is most probably improperly displayed.

Asymptote	State	D_e cm^{-1}	R_e a.u.	B_e cm^{-1}	ω_e cm^{-1}	$\omega_e \chi_e$ cm^{-1}	T_e cm^{-1}	Ref.
Rb$^+(^1S)$ + Ca($4s^2\,^1S$)	$1\,^1\Sigma^+$	3811	7.98	0.034540	74.38	0.31	0	This paper
		3851	7.96	0.034600	73.02		0	[25]
		3717	8.26	0.032371	73.43	0.50	0	[4]
		3714	7.97	0.034735	73.53	0.35	0	[29]
		3666	8.06	0.034100	73.90		0	[28]
		3730	8.00				0	[45]
Rb$^+(^1S)$ + Ca($4s4p\,^3P$)	$1\,^3\Sigma^+$	7559	8.88	0.027877	65.16	0.13	11 288	This paper
		7455	9.15	0.026367	77.92	0.20	10 806	[4]
		7494	8.90	0.027855	64.21	0.16	11 503	[29]
	$1\,^3\Pi$	3195	7.40	0.039834	76.35	0.38	15 692	This paper
		3308	7.63				18 204*	[29] ([4])
		3022	7.38	0.040511	75.86	0.40	15 982	[29]
Rb($5s^2\,S$) + Ca$^+(4s^2\,S)$	$2\,^1\Sigma^+$	1249	12.88	0.013254	30.24	0.15	18 144	This paper
		1284	12.82	0.013388	28.20	0.09	17 764	[4]
		1272	12.86	0.010376	29.89		18 171	[25]
		1160	12.99	0.010376	29.58	0.15	18 015	[29]
		1170	13.00					[45]
	$2\,^3\Sigma^+$ (first min)	−1727	8.32	0.031767	62.14	0.23	21 120	This paper
		−1496	8.31	0.031976			20 128	[4]
		−1839	8.27	0.032261	61.54	0.49	21 014	[29]
	$2\,^3\Sigma^+$ (second min)	181	20.02	0.005488	9.85	0.16	19 212	This paper
		121	17.82				19 018	[4]
		137	20.82	0.005090	8.37	0.13	19 025	[29]
Rb$^+(^1S)$ + Ca($4s3d\,^3D$)	$3\,^3\Sigma^+$	1353	11.54	0.016521	106.02	5.23	22 840	This paper
		1481	11.42	0.016918	61.54	0.49	22 999	[29]
	$2\,^3\Pi$	2894	8.69	0.029145	58.41	0.21	21 299	This paper
		3027	8.67	0.029353	58.30	0.21	21 440	[29]
	$1\,^3\Delta$	3226	8.38	0.031347	62.58	0.22	20 967	This paper
		3293	8.35	0.031646	61.17	0.24	21 189	[29]
Rb$^+(^1S)$ + Ca($4s3d\,^1D$)	$3\,^1\Sigma^+$	2943	8.71	0.028982	60.68	0.22	22 620	This paper
		3175	8.65	0.029489	62.04	0.34	22 835	[29]
	$1\,^1\Pi$	3499	8.42	0.031054	58.39	0.21	22 064	This paper
		3542	8.43	0.031048	57.48	0.16	22 467	[29]
	$1\,^1\Delta$	3981	8.32	0.031772	64.62	0.19	21 582	This paper
		4184	8.29	0.032105	63.51	0.18	21 827	[29]
Rb$^+(^1S)$ + Ca($4s4p\,^1P$)	$4\,^1\Sigma^+$	973	15.01	0.009756	19.42	0.19	25 986	This paper
		1016	14.89	0.009952	22.61	0.31	26035	[29]
	$2\,^1\Pi$	1923	8.46	0.030752	51.10	0.38	25 036	This paper
		1575	8.47	0.030755	46.14	0.51	25 476	[29]
Rb($5p\,^2P$) + Ca$^+(4s^2\,S)$	$5\,^1\Sigma^+$ (first min)	−350	9.59	0.023907	50.28	1.53	32 480	This paper
	$5\,^1\Sigma^+$ (second min)	1216	20.26	0.005343	20.29	0.05	30 914	This paper
		2051	13.61	0.011912	16.90	0.31	30 754	[29]
	$4\,^3\Sigma^+$	1801	18.50	0.006404	18.53	0.04	30 329	This paper
		1745	18.57	0.006398	20.67	0.04	31 163	[29]
	$3\,^1\Pi$	275	12.73	0.013571	16.24	0.52	31 855	This paper
		131	17.00	0.007635	8.70	0.07	31 782	[29]
	$3\,^3\Pi$ (first min)	233	13.48	0.012109			31 897	This paper
	$3\,^3\Pi$ (second min)	281	15.60	0.009032	14.82	0.34	31 849	This paper
		202	16.19	0.008418	12.17	0.16	31 718	[29]
Rb($5s^2\,S$) + Ca$^+(3d\,^2D$)	$6\,^1\Sigma^+$	685	15.40	0.009268	55.72	3.13	32 395	This paper
	$5\,^3\Sigma^+$	937	14.15	0.010978	53.83	2.07	32 143	This paper
	$4\,^1\Pi$	678	14.96	0.009827	25.87	0.33	32 402	This paper
	$4\,^3\Pi$	997	14.00	0.011228	39.73	1.05	32 083	This paper
	$2\,^1\Delta$	1015	13.59	0.011901	27.39	0.16	32 065	This paper
	$2\,^3\Delta$	1162	13.16	0.012701	29.36	0.16	31 918	This paper

+ Ca$^+$(4s ^2S) and Rb$^+$ + Ca(4s4p ^3P) including SOC are expressed as

$$H(\Omega = 0^-) = \begin{pmatrix} V(2\,^3\Sigma^+) & A_{12} & 0 \\ A_{21} & V(1\,^3\Pi) - A_{22} & A_{23} \\ 0 & A_{32} & V(1\,^3\Sigma^+) \end{pmatrix},$$
(A1)

$$H(\Omega = 0^+) = \begin{pmatrix} V(2\,^1\Sigma^+) & A'_{12} \\ A'_{21} & V(1\,^3\Pi) - A'_{22} \end{pmatrix}, \quad (A2)$$

$$H(|\Omega| = 1) = \begin{pmatrix} V(2\,^3\Sigma^+) & A''_{12} & 0 \\ A''_{21} & V(1^3\Pi) & A''_{23} \\ 0 & A''_{32} & V(1\,^3\Sigma^+) \end{pmatrix}, \quad (A3)$$

where the R-dependent coupling terms $A_{ij}, A'_{ij}, A''_{ij}$, are displayed in Fig. 4. Note that we neglected in the $|\Omega| = 1$ matrix [Eq. (A3)] the contribution of the Rb$^+$ + Ca(4s4p ^1P) limit, which is located about 8000 cm^{-1} above the Rb$^+$ + Ca(4s4p ^3P) one. The consequence is that after diagonalization, the energy of Rb$^+$ + Ca(4s4p ^1P) is slightly shifted compared to Rb$^+$ + Ca(4s4p $^3P_{0,2}$) by 0.518 cm^{-1}, which can be neglected in the rest of the paper.

3. Differences between our model and the one of Ref. [27]

To understand the differences between theoretical models, a detailed comparison between the results of this paper and Ref. [27] is presented in Fig. 15. We can see that the dissociation energies of $1\,^3\Pi$ and $2\,^1\Sigma^+$ are close, but the potential

wells differ. Although the SOCs trends are quite different over the short-range <10 a.u., they are similar both at the intersections and at long range. The patterns of the cross section are also consistent as they display a comparable density of shape resonances. Although the difference in the SOC is large at short range, this good agreement also demonstrates that the short-range SOC does not play a role here.

4. Comparison with experimental data

We reported in Fig. 10(b) downscaled experimental data that we obtained by multiplying the measured rate constants in Fig. 6(a) of Ref. [5] by a factor $(1/6) \times (3/4)$. This scaling is reasoned from the following two assumptions reported in Ref. [5]:

(a) the reported experimental data corresponded to the total reaction rate to which the contributions of the Ca$^+$(4s) and Ca$^+$(4p) channels were estimated to be ≈ 1:5.

(b) the ratio of the molecule-formation versus charge-transfer rates was roughly estimated to be ≈ 1:3.

Therefore, a scaling factor of $(1/6) \times (3/4) = 1/8$ yielded a closer match to the theoretical results shown in Fig 10(b). It needs to be emphasized that the channel and product branching ratios reported in Ref. [5] are rough estimations and, consequently, also the relevant scaling factors adapted here need to be treated with caution. Still, an overall scaling of 1/8 of the channel averaged rate constants in Ref. [5] seems to yield acceptable agreement with the presented theoretical values in the lowest collision channel reported in Fig. 10(b).

[1] M. Tomza, K. Jachymski, R. Gerritsma, A. Negretti, T. Calarco, Z. Idziaszek, and P. S. Julienne, Rev. Mod. Phys. **91**, 035001 (2019).

[2] F. H. J. Hall, M. Aymar, N. Bouloufa-Maafa, O. Dulieu, and S. Willitsch, Phys. Rev. Lett. **107**, 243202 (2011).

[3] F. H. J. Hall and S. Willitsch, Phys. Rev. Lett. **109**, 233202 (2012).

[4] F. H. Hall, P. Eberle, G. Hegi, M. Raoult, M. Aymar, O. Dulieu, and S. Willitsch, Mol. Phys. **111**, 2020 (2013).

[5] F. H. Hall, M. Aymar, M. Raoult, O. Dulieu, and S. Willitsch, Mol. Phys. **111**, 1683 (2013).

[6] A. D. Dörfler, P. Eberle, D. Koner, M. Meuwly, and S. Willitsch, Nat. Commun. **10**, 5429 (2019).

[7] A. Mohammadi, A. Krükow, A. Mahdian, M. Deiß, J. Pérez-Ríos, H. da Silva, M. Raoult, O. Dulieu, and J. Hecker Denschlag, Phys. Rev. Res. **3**, 013196 (2021).

[8] S. Haze, R. Saito, M. Fujinaga, and T. Mukaiyama, Phys. Rev. A **91**, 032709 (2015).

[9] R. Saito, S. Haze, M. Sasakawa, R. Nakai, M. Raoult, H. Da Silva, O. Dulieu, and T. Mukaiyama, Phys. Rev. A **95**, 032709 (2017).

[10] J. Joger, H. Fürst, N. Ewald, T. Feldker, M. Tomza, and R. Gerritsma, Phys. Rev. A **96**, 030703(R) (2017).

[11] M. Mills, P. Puri, M. Li, S. J. Schowalter, A. Dunning, C. Schneider, S. Kotochigova, and E. R. Hudson, Phys. Rev. Lett. **122**, 233401 (2019).

[12] M. Li, M. Mills, P. Puri, A. Petrov, E. R. Hudson, and S. Kotochigova, Phys. Rev. A **99**, 062706 (2019).

[13] J. M. Kwolek, D. S. Goodman, B. Slayton, R. Blümel, J. E. Wells, F. A. Narducci, and W. W. Smith, Phys. Rev. A **99**, 052703 (2019).

[14] R. Ben-shlomi, R. Vexiau, Z. Meir, T. Sikorsky, N. Akerman, M. Pinkas, O. Dulieu, and R. Ozeri, Phys. Rev. A **102**, 031301(R) (2020).

[15] A. Krükow, A. Mohammadi, A. Härter, J. H. Denschlag, J. Pérez-Ríos, and C. H. Greene, Phys. Rev. Lett. **116**, 193201 (2016).

[16] A. Krükow, A. Mohammadi, A. Härter, and J. Hecker Denschlag, Phys. Rev. A **94**, 030701(R) (2016).

[17] S. Dutta and S. A. Rangwala, Phys. Rev. A **97**, 041401(R) (2018).

[18] A. Mahdian, A. Krükow, and J. H. Denschlag, New J. Phys. **23**, 065008 (2021).

[19] T. Feldker, H. Fürst, H. Hirzler, N. V. Ewald, M. Mazzanti, D. Wiater, M. Tomza, and R. Gerritsma, Nat. Phys. **16**, 413 (2020).

[20] T. Sikorsky, M. Morita, Z. Meir, A. A. Buchachenko, R. Ben-shlomi, N. Akerman, E. Narevicius, T. V. Tscherbul, and R. Ozeri, Phys. Rev. Lett. **121**, 173402 (2018).

[21] P. Weckesser, F. Thielemann, D. Wiater, A. Wojciechowska, L. Karpa, K. Jachymski, M. Tomza, T. Walker, and T. Schaetz, Nature (London) **600**, 429 (2021).

[22] S. T. Sullivan, W. G. Rellergert, S. Kotochigova, and E. R. Hudson, Phys. Rev. Lett. **109**, 223002 (2012).

[23] S. Jyothi, T. Ray, S. Dutta, A. R. Allouche, R. Vexiau, O. Dulieu, and S. A. Rangwala, Phys. Rev. Lett. **117**, 213002 (2016).

[24] W. G. Rellergert, S. T. Sullivan, S. Kotochigova, A. Petrov, K. Chen, S. J. Schowalter, and E. R. Hudson, Phys. Rev. Lett. **107**, 243201 (2011).

[25] H. da Silva Jr., M. Raoult, M. Aymar, and O. Dulieu, New J. Phys. **17**, 045015 (2015).

[26] J. Szczepkowski, A. Grochola, W. Jastrzebski, P. Kowalczyk, R. Vexiau, N. Bouloufa-Maafa, and O. Dulieu, J. Quant. Spectrosc. Radiat. Transfer **291**, 108330 (2022).

[27] M. Tacconi, F. A. Gianturco, and A. K. Belyaev, Phys. Chem. Chem. Phys. **13**, 19156 (2011).

[28] A. K. Belyaev, S. A. Yakovleva, M. Tacconi, and F. A. Gianturco, Phys. Rev. A **85**, 042716 (2012).

[29] W. Zrafi, H. Ladjimi, H. Said, H. Berriche, and M. Tomza, New J. Phys. **22**, 073015 (2020).

[30] R. Guérout, M. Aymar, and O. Dulieu, Phys. Rev. A **82**, 042508 (2010).

[31] M. Aymar and O. Dulieu, J. Phys. B: At. Mol. Opt. Phys. **45**, 215103 (2012).

[32] B. Huron, J.-P. Malrieu, and P. Rancurel, J. Chem. Phys. **58**, 5745 (1973).

[33] P. Durand and J. Barthelat, Chem. Phys. Lett. **27**, 191 (1974).

[34] I. Schmidt-Mink, W. Müller, and W. Meyer, Chem. Phys. Lett. **112**, 120 (1984).

[35] M. Foucrault, P. Millié, and J. Daudey, J. Chem. Phys. **96**, 1257 (1992).

[36] R. Cimiraglia, J. P. Malrieu, M. Persico, and F. Spiegelmann, J. Phys. B **18**, 3073 (1985).

[37] C. Angeli and M. Persico, Chem. Phys. **204**, 57 (1996).

[38] N. Vanhaecke and O. Dulieu, Mol. Phys. **105**, 1723 (2007).

[39] M. H. Alexander and D. E. Manolopoulos, J. Chem. Phys. **86**, 2044 (1987).

[40] M. Li and B. Gao, Phys. Rev. A **86**, 012707 (2012).

[41] R. Côté and I. Simbotin, Phys. Rev. Lett. **121**, 173401 (2018).

[42] A. Pandey, M. Niranjan, N. Joshi, S. A. Rangwala, R. Vexiau, and O. Dulieu, Phys. Rev. A **101**, 052702 (2020).

[43] A. Kramida, Yu. Ralchenko, J. Reader, and NIST ASD Team, NIST Atomic Spectra Database (ver. 5.9). https://freidok.uni-freiburg.de/data/222424 (accessed Aug. 24, 2022) (National Institute of Standards and Technology, Gaithersburg, MD, 2021).

[44] H. Coker, J. Phys. Chem. **80**, 2078 (1976).

[45] M. Śmiałkowski and M. Tomza, Phys. Rev. A **101**, 012501 (2020).

[46] P. Weckesser, Feshbach resonances between a single ion and ultracold atoms, Ph.D. thesis, Fakultät für Mathematik und Physik, 2021, https://freidok.uni-freiburg.de/data/222424.